

# AI-Driven Robotics for Free-Space Optics

Shiekh Zia Uddin<sup>★, 1,2,\*</sup> Sachin Vaidya<sup>★, 1,2,3,†</sup> Shrish Choudhary,<sup>4</sup> Zhuo Chen,<sup>1,3,5</sup>  
Raafat K. Salib,<sup>4</sup> Luke Huang,<sup>4</sup> Dirk R. Englund,<sup>2,4</sup> and Marin Soljačić<sup>1,2,3</sup>

<sup>1</sup>*Department of Physics, Massachusetts Institute of Technology, Cambridge, Massachusetts 02139, USA*

<sup>2</sup>*Research Laboratory of Electronics, Massachusetts Institute of Technology, Cambridge, Massachusetts 02139, USA*

<sup>3</sup>*The NSF Institute for Artificial Intelligence and Fundamental Interactions*

<sup>4</sup>*Department of Electrical Engineering and Computer Science,*

*Massachusetts Institute of Technology, Cambridge, Massachusetts 02139, USA*

<sup>5</sup>*Institute for Data, Systems and Society, Massachusetts Institute of Technology, Cambridge, MA 02142*

<sup>★</sup> *denotes equal contribution*

Tabletop optical experiments are foundational to research in many areas of science, including photonics, quantum optics, materials science, metrology, and biomedical imaging. However these experiments remain fundamentally reliant on manual design, assembly, and alignment—limiting throughput and reproducibility. Optics currently lacks generalizable robotic systems capable of operating across a diverse range of setups in realistic laboratory environments. Here we present OptoMate, an autonomous platform that integrates generative AI, computer vision, and precision robotics to enable automation of free-space optics experiments. Our platform interprets user-defined goals to generate valid optical setups using a fine-tuned large language model (LLM), assembles the setup via robotic pick-and-place with sub-millimeter accuracy, and performs fine alignment using a robot-deployable tool. The system then executes a range of automated measurements—including laser beam characterization, polarization mapping, and spectroscopy tasks. This work demonstrates the first flexible, AI-driven automation platform for optics, offering a path toward remote operation, cloud labs, and high-throughput discovery in the optical sciences.

The precise and repeatable control of experimental workflows is a central challenge across the physical sciences. In recent years, the proliferation of data-driven methods and large-scale artificial intelligence (AI) have been transforming how measurements are planned, executed and interpreted [1–3]. As AI-enabled approaches become more pervasive, the need for integrated automation in bench-scale experiments has grown ever more urgent. Pioneering efforts in other fields have already demonstrated the utility of robotics in accelerating scientific progress. In chemistry, automated platforms now execute multi-step syntheses and characterize reaction outcomes with minimal human intervention, enabling rapid exploration of chemical space [4–8]. Similarly, programmable fabrication systems have been harnessed to synthesize materials with targeted properties, perform manipulations with atomically precise control and perform characterization tasks [9–12], while cloud-based laboratories offer remote access to state-of-the-art instrumentation at large scales [13].

Despite successes in other disciplines, the field of optics has remained predominantly manual in its implementation. While recent studies have explored the use of AI to discover or optimize optical configurations [14–17], the development of a fully autonomous, end-to-end pipeline from design to implementation remains a challenge. This inertia stems from challenges intrinsic to free-space optical systems, which demand reconfigurability, sub-micron precision in alignment, continuous tuning of sensitive optical elements, and in-situ diagnostics that are highly susceptible to environmental fluctuations.

Meeting these stringent demands requires an interdisciplinary approach—one that integrates AI, precision robotics, computer-vision, engineering, and deep expertise in optical systems. An AI-driven robotic framework for optics could overcome these limitations, significantly accelerating experimental workflows. Such a framework would also expand accessibility to complex optical experiments and allow for the exploration of the vast space of optical configurations.

Here, we address this critical gap by introducing OptoMate—an AI-driven robotics platform for free-space optics (Figure 1). OptoMate aims to automate the three fundamental stages of an optical experiment: (1) the design of optical setups, (2) the physical assembly and fine alignment of components, and (3) the execution of measurements. At the design stage, we employ fine-tuned large language models (LLMs) that interpret user-specified goals and generate valid optical setups within the physical constraints of the laboratory environment. These LLM-generated setups are translated into robot control code using a second LLM-based agent. A robotic arm equipped with a computer vision system then performs pick-and-place operations with sub-millimeter precision, followed by fine alignment using a robot-deployable tool. In the final stage, we demonstrate a range of automated measurements commonly performed in optics—including beam characterization, polarization mapping, and transmission spectroscopy.

## I. OPTICAL SETUP GENERATION USING LLMs

Designing optical setups requires awareness of laboratory spatial constraints, and the ability to translate experimental

\* suddin@mit.edu

† svaidya1@mit.edu

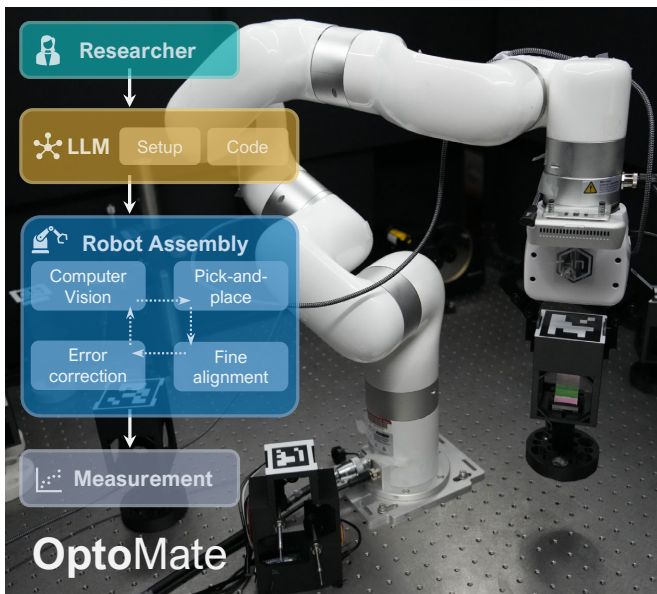


**Figure 1. Overview of OptoMate.** A researcher specifies goals for optics experiments, which are interpreted by a large language model (LLM) to generate structured optical setups and executable code. A robotic arm equipped with computer vision then performs optical component identification, pick-and-place operations, positional error correction and fine alignment. Once assembled, the platform performs optical measurements without human intervention.

goals into executable configurations. Traditionally, this process is time-intensive, reliant on expertise, and often involves numerous iterative refinements. As the first stage in the automation pipeline, we present a large language model (LLM)-driven system that automates optical setup design by translating natural language descriptions into valid, spatially-aware, and executable optical setups (Figure 2a).

To demonstrate the system’s capabilities, we focus on four canonical optical setups of varying complexity: Michelson interferometer, Mach-Zehnder interferometer, Hong-Ou-Mandel interferometer, and a 4f optical imaging system. Each setup is defined as a list of tuples, with each tuple encoding an optical component ID, x-y position, and orientation. We assume all components to have a fixed z-position (height). From a single reference of each setup, we generate a dataset through geometric data augmentation using similarity transformations—translations, scalings, rotations, and reflections. These synthetic setups are subsequently filtered to ensure physical feasibility: they must lie entirely within the robot-accessible workspace, have no overlapping components, and avoid internal beam paths intersecting the robotic arm’s footprint (for details see Methods).

For each valid setup in the dataset, we generate natural language descriptions using an auto-captioning step. These captions simulate user inputs with varying degrees of specificity, ranging from high-level objectives (e.g., “Give me a Mach-

Zehnder interferometer”) to setups with specific requirements (e.g., “Give me a Michelson interferometer setup. The incoming laser beam direction makes an angle of 30 degrees with the x-axis and the setup should have a beamsplitter positioned at approximately (20 cm, 3 cm)”).

We fine-tune a pretrained LLaMA3.1-8B-Instruct model for this task using Quantum-informed Tensor Adaptation (QuanTA) [18], a parameter-efficient fine-tuning (PEFT) method (see Methods). QuanTA utilizes quantum-inspired tensor networks to modify model weights, enabling efficient high-rank adaptations that can capture complex structural relationships while using significantly fewer trainable parameters than full fine-tuning. Our fine-tuning strategy involves two sequential stages: first, we train the model on our augmented dataset to learn the fundamental principles of generating physically valid optical layouts (structure learning); second, we continue the training with prompts containing specific user constraints to enhance the model’s ability to interpret and adhere to precise experimental requirements (user request understanding). Once the LLM generates an optical setup, a validation step evaluates the geometric and physical feasibility of the layout (see Methods). If the configuration fails this validation, it is returned to the model for refinement in a closed-loop correction process. Validated setups are then passed to a secondary LLM-based agent (based on Claude 3.7) which translates the symbolic layout into executable robotic movement commands for physical assembly in the laboratory (see Methods) (Figure 2a).

To assess the effectiveness and necessity of our fine-tuning approach, we compare QuanTA with three alternative strategies: (1) zero-shot inference using GPT-4o, (2) prompt-engineered GPT-4o, and (3) prompt engineering combined with chain-of-thought reasoning using DeepSeek R1 (Figure 2b). We find that our fine-tuned model achieves the highest pre-validation accuracy and the greatest compliance with user-specified constraints. While all approaches ultimately produce a valid setup after iterating through the validation step, the lower pre-validation accuracies of the other methods translate directly into significantly higher computational costs, greater token usage per valid setup, and increased time required to generate a correct solution, compared to fine-tuning.

## II. ROBOTIC ASSEMBLY AND FINE ALIGNMENT OF OPTICAL SETUPS

Following the generation of valid and spatially aware optical setups by the LLM-based design system, the next stage involves the autonomous assembly and fine alignment of these setups using a robotic platform. This system is built around a 7-degree-of-freedom robotic arm (UFACTORY xArm7) with measured spatial and angular precisions for placement of  $\pm 0.5$  mm and  $0.2^\circ$  respectively, a payload capacity of 3.5 kg, and a reach radius of 61 cm. The arm is programmed to perform high-precision placement of optical components, including mirrors, lenses, beam splitters, and detectors. The robotic platform integrates computer vision, LiDAR-based scanning and depth

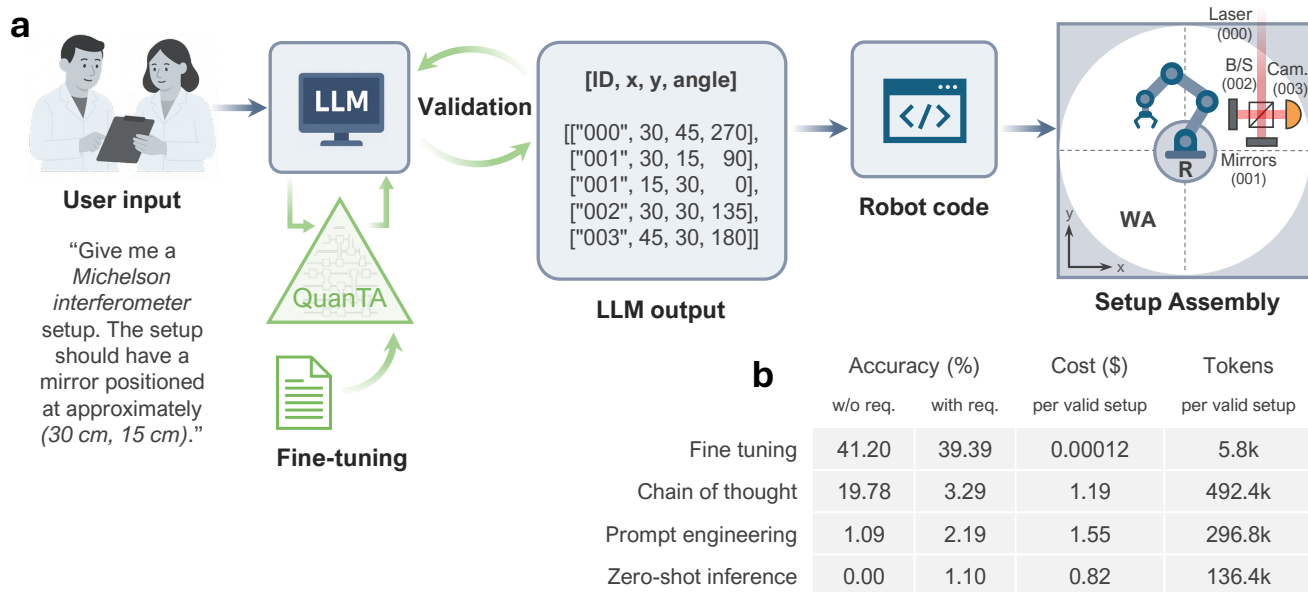


**Figure 2. Optical setup generation using fine-tuned large language models.** A researcher provides a natural language input for the desired optical setup. A large language model, fine-tuned using QuanTA [18], generates optical setups. An optical setup includes component IDs, spatial coordinates, and orientations of all components that comprise the setup. This structured output is validated for accuracy and physical feasibility and translated into robot-executable code for assembly. The last panel shows a schematic of a generated setup in the laboratory space, where “R” denotes the footprint of the robotic arm and “WA” indicates the working area of the robotic arm. **(b)** Comparison of prompting strategies for optical setup generation. Accuracy is reported both with and without user-specified constraints or requests (denoted as “with req.” and “w/o req.”, respectively). Cost and token usage are shown as averages, computed based on the “with req.” accuracy values (1k = 1,000; \$ = USD). Fine-tuning with QuanTA achieves the highest accuracy with significantly better cost and token efficiency, outperforming chain-of-thought reasoning, prompt engineering, and zero-shot inference.

sensing, and custom-designed optical component holders and magnetic bases, all optimized for robotic manipulation.

Each optical component is placed in a 3D-printed housing designed to universally fit standard off-the-shelf optical components and is placed in a 3D-printed base with magnets that provide resistance to unwanted motion during assembly and alignment (Figure 3a). The housing has an ArUco fiducial marker affixed to the top surface that facilitates component identification and positioning via stereo 4K visible-light cameras mounted around the workspace. These cameras perform an initial scan of the optical table, allowing the system to estimate component positions and orientations. Once a candidate component is identified, the robotic arm approaches it, and a LIDAR sensor mounted on the end-effector performs a high-resolution scan to refine the object’s pose and geometry. This multi-modal perception pipeline ensures sub-millimeter grasping accuracy and minimizes the risk of collision or misplacement. Upon successful pickup, components are placed at their target positions and orientations according to the layout provided either by a user or by the fine-tuned LLM (see Supplementary Videos 1 and 2). During placement, an error correction step ensures both positional and angular fidelity by rechecking these parameters using the computer vision system.

For optical setups requiring precision beyond the capabilities of initial placement, we develop a robot-deployable fine

alignment tool (Figure 3b, also see Supplementary Video 9). This compact, motorized device is constructed to interface with the fine-adjustment knobs located on standard optical mounts, providing electronically controlled, micrometer-scale adjustments to the component’s degrees of freedom. The tool consists of an Arduino Nano microcontroller, a custom PCB with integrated motor drivers, precision-machined Allen keys mounted on low-friction bearing-supported motor shafts, and a dedicated camera and LED illumination system embedded within the housing. For fine alignment tasks, the robotic arm autonomously picks up the fine alignment tool and inserts the Allen keys of the tool into the adjustment knobs of optical components requiring alignment. Accurate insertion is enabled by cameras and LEDs located inside the tool, along with a second ArUco marker on the side surface of the component housing. Alignment adjustments are performed iteratively, guided by feedback from cameras or photodetectors previously placed along the beam path, either through an alignment algorithm or under remote user control. The complete robotic pipeline is shown schematically in Figure 3c (see Methods for more details on the computer vision system, robot pick-and-place operations, custom housing and bases, construction of fine-alignment tool, and correction of positional errors).

To demonstrate the capabilities of the robotic assembly and fine-alignment system, we autonomously construct and align

a Michelson interferometer from scratch (Figure 3d, also see Supplementary Videos 3 and 4). The optical layout for the interferometer is generated by the fine-tuned LLM in response to a user-specified constraint on the incoming laser beam direction. Based on the generated design, the computer vision system identifies the required components — two mirrors, a beam splitter, and a camera — and the robotic arm subsequently places them on the optical table (Figure 3d). Following initial assembly, the robotic arm deploys the fine-alignment tool to iteratively adjust the orientation of the mirrors, ensuring the precise overlap of the two beams of the interferometer. Feedback for the alignment is obtained by blocking each arm and centering the beams in the camera’s field of view. The final interferometer and the resulting stable interference pattern are shown in Figure 3d.

### III. AUTOMATED OPTICAL MEASUREMENTS

Following the successful autonomous assembly and fine alignment of optical setups, we proceed to executing automated optical measurements with our platform. While the assembly process involves static placement of components, many optical experiments require dynamic operations such as translating, rotating, or adjusting optical elements in real time. These dynamic measurement tasks demand the same level of precision, robustness, and autonomy as the assembly process, but introduce additional challenges related to motion control. Moreover, measurements are also integral to the assembly phase itself—for instance, verifying laser alignment, and characterizing beam quality during setup construction. Thus, the integration of real-time optical diagnostic and measurement capabilities is critical to achieving fully autonomous experimentation.

Leveraging the robotic platform’s ability to manipulate optical elements with high spatial and angular accuracy, we demonstrate automated execution of optical measurements. In this section, we show this functionality across four examples of distinct measurement tasks: (1) beam direction and waist tracking, (2) beam quality characterization through beam matrix measurement, (3) polarization mapping via spatially resolved Stokes parameter extraction, and (4) angle- and wavelength-resolved spectroscopy of multilayer photonic crystals.

To determine the propagation direction of a collimated laser beam, the robotic arm picks up a camera module and positions it such that the beam is centered within the field of view. The robotic arm then translates the camera while keeping the beam centered in the camera’s field of view. By recording the beam centroid through this motion, the beam’s angle relative to the laboratory axes is calculated using a linear regression fit (see Supplementary Video 5). Similarly, the beam waist can be directly measured from the camera images. In a typical configuration, beam angles along the  $x$ ,  $y$ , and  $z$  axes are measured to be  $88.16^\circ \pm 0.05^\circ$ ,  $89.16^\circ \pm 0.05^\circ$ , and  $2.03^\circ \pm 0.04^\circ$ , respectively, averaged over 230 measurements (Figure 4a).

Precise spatial characterization of laser beams is essential

in a wide range of experiments, from beam shaping and mode matching to the calibration of complex optical systems. The complete spatial characterization of the beam can be determined via a measurement of the second-order moments of the Wigner distribution, commonly referred to as the beam matrix, which represent the beam’s spatial intensity and phase in both position and momentum (or angle) space. This matrix records beam properties such as width, divergence, astigmatism, and ellipticity. The components of the beam matrix can be measured by imaging the beam at different planes along the propagation axis and at different positions using cylindrical and spherical lenses and a camera.

To measure the beam matrix, the robotic arm places down a camera and translates a lens in the beam path, capturing the transverse intensity profile at multiple propagation distances (see Supplementary Video 6). From these images, second-order spatial and angular moments are computed, yielding a full  $4 \times 4$  beam matrix (Figure 4b):

$$M = \begin{pmatrix} \langle x^2 \rangle & \langle xy \rangle & \langle x\theta_x \rangle & \langle x\theta_y \rangle \\ \langle xy \rangle & \langle y^2 \rangle & \langle y\theta_x \rangle & \langle y\theta_y \rangle \\ \langle \theta_x x \rangle & \langle \theta_x y \rangle & \langle \theta_x^2 \rangle & \langle \theta_x \theta_y \rangle \\ \langle \theta_y x \rangle & \langle \theta_y y \rangle & \langle \theta_x \theta_y \rangle & \langle \theta_y^2 \rangle \end{pmatrix} = 10^{-7} \begin{pmatrix} 0.13 \text{ m}^2 & 0.06 \text{ m}^2 & 0.08 \text{ m} & -0.02 \text{ m} \\ 0.06 \text{ m}^2 & 0.12 \text{ m}^2 & 0.27 \text{ m} & 0.00 \text{ m} \\ 0.08 \text{ m} & 0.27 \text{ m} & 2.80 & 0.04 \\ -0.02 \text{ m} & 0.00 \text{ m} & 0.04 & 3.06 \end{pmatrix}$$

Here,  $x$  and  $y$  are the spatial coordinates of the beam, and  $\theta_x$  and  $\theta_y$  are the angular divergences in the  $x$  and  $y$  directions, respectively. The diagonal elements describe the beam’s spread (e.g.,  $\langle x^2 \rangle$  is the beam width in the  $x$ -direction), while the off-diagonal elements describe correlations between position and angle or between different spatial directions. The effective beam propagation ratio is measured to be  $M_{\text{eff}}^2 = \frac{4\pi}{\lambda} [\det M]^{1/4} = 1.07 \pm 0.03$ , where  $\lambda = 632.8 \text{ nm}$  is the wavelength of light.

We next turn our attention to the characterization of spatially varying polarization fields, which is essential for identifying polarization singularities and vectorial field distributions in beam optics applications. To show this functionality the robotic arm assembles a setup consisting of a linear polarizer and camera and then inserts and rotates a quarter-wave plate (QWP) along the beam path (see Supplementary Video 7). The intensity at each camera pixel  $I(\theta)$  as a function of QWP angle  $\theta$  follows:

$$I(\theta) = \frac{1}{2} (S_0 + S_1 \cos^2 2\theta + S_2 \sin 2\theta \cos 2\theta + S_3 \sin 2\theta)$$

By fitting this expression at each pixel, the spatially resolved Stokes parameters  $S_0, S_1, S_2, S_3$  are extracted. From these, the degree of polarization and the orientation of polarization ellipses are computed and superimposed on the beam intensity image (Figure 4c).

Finally, we demonstrate automated angle-resolved spectral characterization of multilayer photonic crystals, a task com-

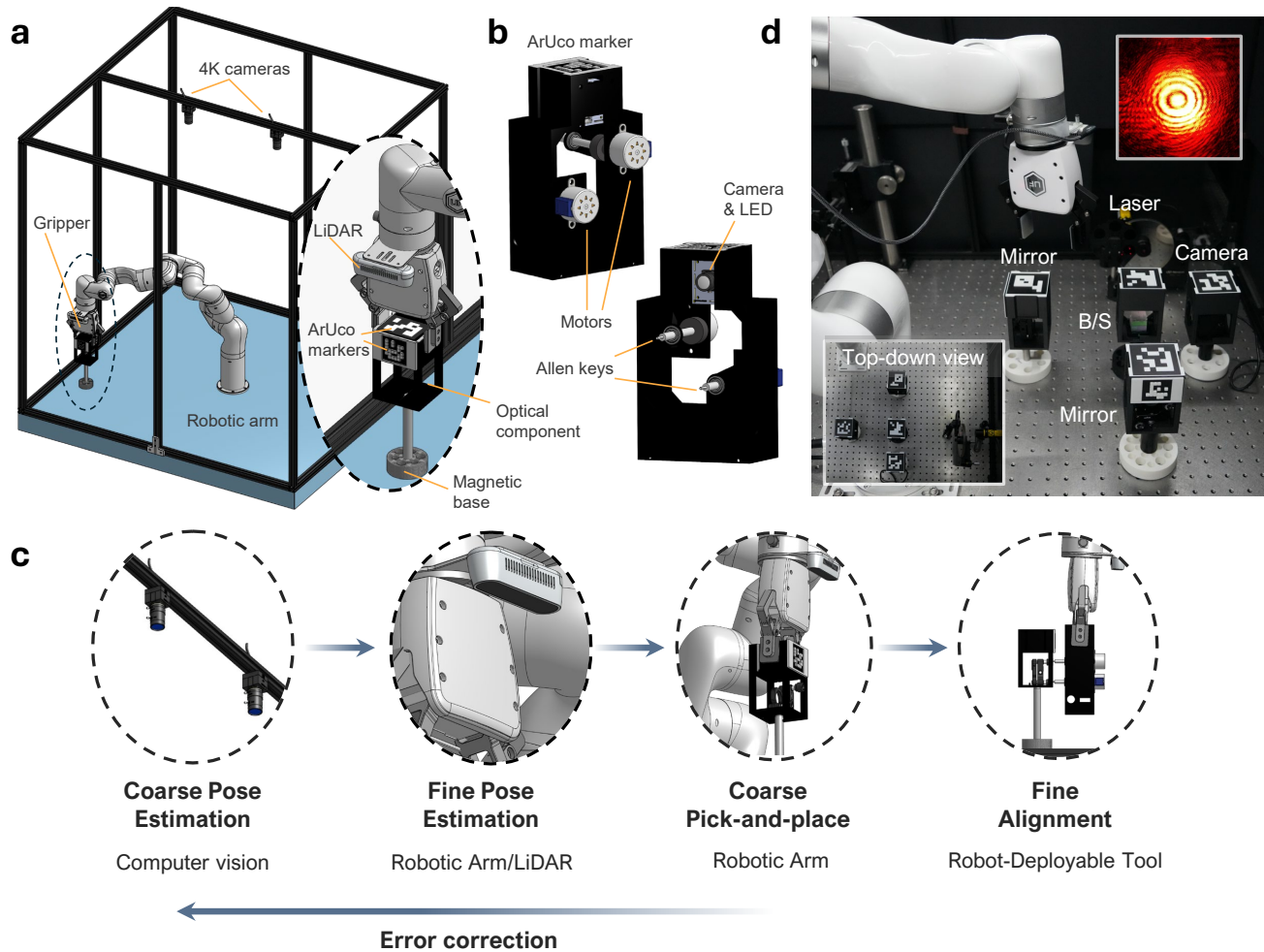


**Figure 3. Robotic platform for autonomous assembly and alignment of optical setups.** (a) Schematic of the robotic platform, consisting of a 7-degree-of-freedom robotic arm equipped with a gripper and a LiDAR camera, as well as external 4K cameras mounted around the workspace to provide stereo vision. Optical components are housed in custom 3D-printed casings labeled with ArUco fiducial markers for identification and positioning. The components are placed in 3D-printed magnetic bases that resist unwanted motion during handling. (b) A schematic of the robot-deployable fine-alignment tool, which consists of two motors with Allen keys mounted on their shafts and an onboard computer vision system enabled by a camera and a white-light LED. (c) Pipeline for autonomous assembly of optical setups. First, the computer vision system performs a coarse estimation of the location, orientation, and angles of the components in the working area using the 4K cameras. The robotic arm then refines this estimate using the onboard LiDAR sensor. Next, a coarse pick-and-place operation positions and orients the component as desired within the optical setup, achieving sub-millimeter and sub-degree precision. Finally, the robot-deployable fine-alignment tool executes micro-adjustments, achieving the sub-arcminute angular precision required for functional optical alignment. This multi-stage pipeline enables robust and repeatable assembly of complex free-space optical configurations. (d) Autonomously assembled and aligned Michelson interferometer setup in the laboratory. The insets show a top-down view of the interferometer and a camera image of the achieved interference pattern.

monly performed to measure the bands of periodic photonic materials. This measurement typically requires precise and repeatable angular sweeps, making them labor-intensive and sensitive to alignment errors when performed manually. The robotic arm first assembles a setup consisting of a diffraction grating and a camera positioned along the path of a supercontinuum (SC) laser beam. It then picks up a multilayer photonic crystal (consisting of alternating layers of Si and SiO<sub>2</sub> with an embedded defect layer to form a cavity) housed in a 3D-printed casing.

The arm then rotates the photonic crystal through a range of incidence angles (see Supplementary Video 8). At each angle, the transmission spectrum is recorded, yielding the complete wavelength- and angle-resolved transmission spectrum (Figure 4d) (see Methods for more details).

These four demonstrations collectively highlight the flexibility of robotic systems for executing high-precision optical measurements. Together, they establish that a robotic arm can serve as a versatile experimental tool in optics and photonics,

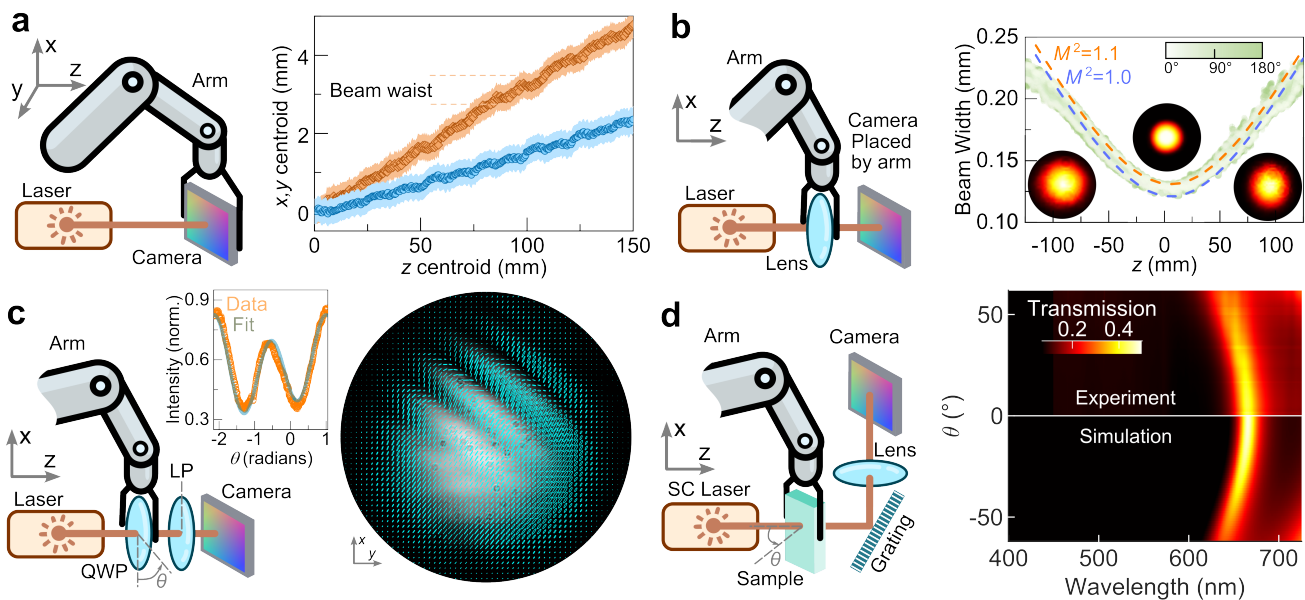


**Figure 4. Automated optical measurements and characterization tasks.** (a) The robotic arm linearly moves a camera, tracking the centroid of the laser beam to measure its direction and width. (b) The robotic arm places a lens in the beam path and moves the camera in the z-direction, capturing images. This data is used to calculate the beam matrix. (c) The robotic arm assembles a setup consisting of a camera and a linear polarizer (LP) in the beam path. The beam passes through a birefringent film (BRF), creating spatial variations in the polarization. The robotic arm holds a quarter-wave plate (QWP) and rotates it, while the camera captures images. These images are used to calculate the Stokes parameters and plot polarization ellipses superimposed on the intensity image. (d) The robotic arm assembles a setup consisting of a grating and a camera to create a spectrometer and then holds and rotates a multilayer photonic crystal to obtain the angle- and wavelength-resolved transmission spectrum.

effectively replacing a range of custom, purpose-built characterization instruments with a single reconfigurable platform.

#### IV. DISCUSSION AND CONCLUSION

We have demonstrated the feasibility and effectiveness of an AI-driven robotic platform for optical setup design, assembly, alignment, and measurement. By integrating artificial intelligence, a robotic arm equipped with multimodal computer vision, and modular alignment tools, we have established the first complete automation pipeline that substantially reduces the need for manual intervention in optics laboratories.

For LLM-based optical setup generation, we have shown that our fine-tuning approach significantly outperforms conventional prompt-engineering-based or zero-shot methods with respect to physical validity, user compliance, and cost- and token-efficiency. This indicates that domain-specific fine-tuning, combined with structural constraints, can produce models capable of reasoning over physically grounded design spaces—a capability of increasing importance for AI-assisted experimentation.

The robotic assembly and alignment system addresses a persistent bottleneck in optics: the precise placement and alignment of free-space optical components. Our demonstration of automated optical measurements—including beam

characterization, polarization mapping, and spectroscopy tasks—illustrates the breadth of tasks amenable to full automation. These examples represent generalizable workflows that can be extended to material characterization, imaging applications, and remote beam monitoring, particularly in hazardous environments such as high-power laser and X-ray facilities.

Looking ahead, several opportunities exist to further enhance this platform. One promising direction is the incorporation of reinforcement learning algorithms for setup alignment and real-time optimization under experimental conditions. This is particularly relevant in optics, where the reward signal can be sparse and highly intermittent during alignment, posing a challenge well-suited to reinforcement learning techniques. Another avenue is the integration of simulation-in-the-loop frameworks, where optical modeling tools inform both LLM-based setup generation and robotic execution. Finally, cloud-based deployment would enable distributed and democratized access to advanced optical experimentation.

#### V. ACKNOWLEDGMENTS

We acknowledge support from the National Science Foundation under Cooperative Agreement PHY-2019786 (The NSF AI Institute for Artificial Intelligence and Fundamental Inter-

actions). S.C., R.K.S. and L.H. acknowledge funding from the MIT Undergraduate Research Opportunities Program (UROP). Z.C. acknowledges support from the Mathworks Fellowship. This work is also supported in part by the U. S. Army Research Office through the Institute for Soldier Nanotechnologies at MIT, under Collaborative Agreement Number W911NF-23-2-0121. The computations in this paper were partly run on the FASRC Cannon cluster supported by the FAS Division of Science Research Computing Group at Harvard University, We also acknowledge support of Parviz Tayebati.

## VI. AUTHOR CONTRIBUTIONS

M.S., S.V. and S.Z.U. conceived the original idea with input from D.R.E.; S.Z.U., S.C., R.K.S., and S.V. developed the robotic platform; S.Z.U., S.C. and R.K.S. performed all experiments and measurements with input from S.V. and L.H.; Z.C. and S.V. generated the optical setup dataset, performed fine tuning of the LLMs and validation of generated setups. The manuscript was written by S.V. and S.Z.U. with inputs from all authors. M.S. supervised the project.

## VII. DATA AVAILABILITY

The data and codes that support the plots within this paper and other findings of this work are available from the corresponding authors upon reasonable request. Correspondence and requests for materials should be addressed to S.Z.U. (sudin@mit.edu) and S.V. (svaidya1@mit.edu).

## VIII. CONFLICT OF INTEREST

S.Z.U., S.V., S.C., R.K.S., L.H. and M.S. are seeking patent protection for some ideas in this work (U.S. provisional patent application no. 63/745, 115). The remaining authors declare no conflicts of interest.

## IX. SUPPLEMENTARY MATERIAL: VIDEOS

The following videos show key capabilities of the robotic system; click the embedded links to view them.

- [Video 1](#): Pick-and-place of optical components
- [Video 2](#): Repeated and consistent pick-and-place of components
- [Video 3](#): Assembly and teardown of LLM-generated Michelson interferometers.
- [Video 4](#): Complete assembly and fine alignment of a Michelson interferometer.

- [Video 5](#): Measurement of beam direction and width.
- [Video 6](#): Measurement of beam  $M^2$ .
- [Video 7](#): Polarization mapping measurement.
- [Video 8](#): Measurement of angle-resolved transmission spectrum of a photonic crystal.
- [Video 9](#): CAD model of the robot-deployable fine-alignment tool.

## X. METHODS

### A. Optical setup dataset generation

To construct a diverse and laboratory aware dataset of optical layouts, we develop a data augmentation pipeline centered around a library of canonical optical setups: Michelson interferometer, Mach-Zehnder interferometer, Hong-Ou-Mandel interferometer and a 4f optical system. Each setup is encoded as a list of component tuples—each specifying a component ID (e.g., mirror, beamsplitter), spatial coordinates (x, y in cm), and optical axis orientation (in degrees). We assume all components to have a fixed height in the z-direction. The first tuple with the component ID “000” is always a ray representing the incoming laser beam. The spatial coordinates within this tuple are those of any point lying on the ray and the orientation component is its angle with the x axis.

To expand this initial set and introduce geometric variability, we applied randomly chosen similarity transformations to each reference layout. Specifically, for each predefined reference setup, we generated multiple setups via random combinations of scaling, in-plane rotation, translations, and mirroring across the x- and/or y-axis. Each transformation was applied to the full component list, updating both spatial coordinates and optical axis orientations accordingly.

Resulting setups were subjected to rigorous physical validation to ensure experimental feasibility. Validation criteria included: (1) all components must lie within the reachable circular workspace of a 61 cm radius; (2) no component may intersect the robot’s 15 cm radius circular footprint at the origin; (3) inter-component spacing must exceed individual component dimensions (7.5 cm  $\times$  6.4 cm) to avoid spatial overlap; and (4) internal beam paths must not intersect the robotic arm’s footprint, determined by constructing a complete graph from the component coordinates and checking for overlap. Setups failing any of these constraints were discarded.

### B. LLM Fine tuning

To enable the translation of natural language experimental goals into precise and structured optical layouts, we fine-tuned the LLaMA3.1-8B-Instruct model using a parameter-efficient fine-tuning (PEFT) strategy. Specifically, we em-

ployed Quantum-informed Tensor Adaptation (QuanTA) [18], a method inspired by quantum circuit structures and tensor networks that enables efficient high-rank updates to pre-trained model weights. Compared to conventional low-rank adaptation methods, QuanTA offers increased representational capacity with comparable computational efficiency, making it well-suited for capturing the complex structural and geometric constraints inherent to optical setup design.

A consistent system prompt was employed throughout both the fine-tuning and inference stages to clearly define the task scope, specify the desired output format (structured lists of component tuples: ID, x, y, orientation), and impose fundamental constraints such as workspace boundaries and component non-overlap. Full details of the system prompt and dataset specifications are provided in the Supplementary Material.

Our fine-tuning protocol involved two sequential stages: *Structure Learning* – In the first stage, the LLaMA3.1-8B-Instruct model, initialized with the system prompt, was fine-tuned on a dataset (described above) comprising pairs of auto-captioned natural language descriptors and their corresponding structured optical layouts. The primary goal of this stage was to enable the model to produce syntactically correct and physically plausible component arrangements, consistent with the basic spatial rules defined during dataset generation.

*User Request Understanding* – Following the initial structure learning, the model underwent further fine-tuning using prompts representing more specific user requests, such as prescribed component positions or beam path characteristics (e.g., “Generate a Michelson interferometer setup with the incoming laser beam at 30 degrees relative to the x-axis”). While the target outputs remained structured component lists, the prompts introduced more nuanced constraints, improving the model’s ability to flexibly interpret and satisfy user-defined experimental requirements.

To establish baseline performance benchmarks, we evaluated two contemporary large language models: GPT-4o and DeepSeek R1. For the GPT-4o model, we assessed performance under two distinct prompting conditions: (1) zero-shot prompting, providing the model solely with the user request and the required output format specification, and (2) few-shot prompting, augmenting the prompt with illustrative examples of both valid and invalid optical layouts. For the DeepSeek R1 model, we employed a few-shot Chain-of-Thought (CoT) prompting. This approach was structured to guide the model through step-by-step reasoning for optical layout construction, supported by representative examples. The accuracy of all evaluated approaches was measured against a newly generated test dataset, utilizing a generation temperature of 0.5 to moderate output randomness. Further comparative analyses of model performance and detailed descriptions of the prompt engineering techniques are documented in the Supplementary Material.

### C. Validation of optical setups

To ensure that optical setups generated by the LLM are accurate and adhere to physical and geometric constraints, we employ a validation procedure that extends the checks used during synthetic dataset generation. First, we apply a set of rule-based spatial constraints to the model-generated setup: all components must lie within the robot’s 61 cm radius reach, remain outside the 15 cm radius circular footprint of the robot at the origin, maintain non-overlapping placement based on their 7.5 cm  $\times$  6.4 cm physical dimensions, and internal beam paths must not intersect the robotic arm’s footprint.

Passing these spatial checks does not guarantee that the laser beam will correctly propagate through the setup, as the component orientations or positions may still be physically inaccurate. To address this, we perform an additional validation step that verifies the structural correctness of the generated setup against a known reference. We do this by attempting to identify a similarity transformation that maps the LLM-generated setup onto one of the predefined reference setups of the same type. This is framed as a geometric alignment task, where the candidate transformation must preserve component identities and maintain approximate spatial relationships within tolerance bounds. If such a transformation exists, the generated setup is deemed valid due to its equivalence to the corresponding reference configuration. This step ensures that the model has not only obeyed spatial constraints but also produced a layout that structurally corresponds to an accurate optical arrangement of components. Furthermore, this allows us to benchmark and test the accuracy of LLM-generated setups with various prompting strategies (Figure 2b of the main text).

### D. Generation of robot motion code

In this part of our workflow, we utilize Claude 3.7, a large language model, to transform high-level interferometer design specifications into executable robotic control code. By leveraging pre-defined wrapper functions that discretize the optical assembly task, we translate the design parameters directly into robotic instructions systematically. The process involves providing Claude 3.7 with a list of tuples with component specifications in the format [component ID, x position, y position, orientation angle] from the LLM design alongside a mapping between component identifiers and their corresponding ArUco markers of the hardware for computer vision recognition. After describing the system’s functional capabilities through four wrapper functions (system initialization, component pickup via visual recognition, precise placement, and robotic arm homing), Claude generates a Python main function that systematically processes the interferometer design. The resulting code initializes the vision and robotic systems, parsed the design data, appropriately filtered non-robotic components, and implements an assembly sequence that handles component identification, retrieval, pre-

cise placement, and safe arm positioning between operations, and achieves the specified optical geometry specified by the LLM optical design. The prompt and example code are provided in the Supplementary Material.

### E. Computer vision system

The robotic system’s vision pipeline is built around a stereo vision setup composed of two 4K ELP cameras mounted 23 cm apart. Initial calibration is conducted using a standard checkerboard pattern, with images collected at varying positions on the optical workbench. Intrinsic and extrinsic parameters of the stereo pair are obtained using the OpenCV `cv2.calibrateCamera` and `cv2.stereoCalibrate` functions. The calibration outputs are validated by comparing the predicted baseline offset to the physical camera separation, confirming sub-millimeter discrepancies. These calibration parameters are stored in a serialized NumPy archive (`stereo_calibration2.npz`) for use in subsequent 3D position estimations during coarse alignment operations.

To enable robust and accurate object detection, we employ the ArUco fiducial markers. Each optical component is tagged with a unique identifier drawn from a 6×6 binary dictionary comprising over 800 distinguishable codes. These tags are detected using the `cv2.aruco` module, which computes the component’s pose via the `cv2.solvePnP` algorithm using previously derived camera intrinsics. While the  $x$  and  $y$  positional estimates from ArUco detection are sufficiently accurate for coarse positioning, the  $z$ -coordinate is instead inferred from a depth measurement. For this, we deploy a robot-mounted Intel RealSense depth camera equipped with LiDAR. After the ArUco tag is centered in the camera field of view, the LiDAR sensor provides a high-accuracy depth estimate, enabling precise  $z$ -coordinate acquisition. The robot’s end-effector is then translated vertically from a known camera-to-gripper offset to achieve accurate engagement with the object.

The precision and robustness of this system allow for successful detection and manipulation even with smaller ArUco tags, as demonstrated in the fine alignment tool deployment. To facilitate consistent image acquisition, the workspace is illuminated with diffuse white-light LED strips integrated into the overhead structure. Additional directional LEDs are positioned in the fine-alignment tool to enhance tag visibility. To suppress glare and reduce errors from ambient light sources, light-blocking panels are installed around the frame perimeter.

To support micro-scale adjustments, we developed an auxiliary vision routine dedicated to centering the fine-alignment tool. An ArUco marker affixed to the housing of the tool is tracked to guide lateral adjustments, aligning the tool precisely with rotational knobs or alignment targets. This system has been validated across a range of component geometries and operates reliably under varied lighting conditions.

A potential limitation of the current implementation is the need for uniquely assigned ArUco tags across all components. In practice, this is mitigated by the large dictionary size and

spatial separation of simultaneously visible tags. In multi-robot configurations, each robot can utilize a dedicated camera and ArUco ID space, supporting scalability for distributed collaboration in large or reconfigurable optical assemblies.

### F. Optical component casing and bases

To facilitate reliable robotic handling of diverse optical components, we designed and fabricated universal housings and bases using fused deposition modeling (FDM) 3D printing with polylactic acid (PLA) filament using the Bambu X1E 3D printer. Each housing is tailored to securely enclose optical components, while presenting a standardized external geometry. This uniformity eliminates the need for the robotic arm to adapt dynamically to variations in component shapes and sizes, simplifying grasping and manipulation.

An indentation feature is incorporated into each housing, precisely aligned to the robot’s claw gripper dimensions. This design ensures repeatable, stable engagement of the gripper during pickup and transport, significantly reducing the likelihood of slippage or misalignment during handling.

For optical component positioning and identification, an ArUco fiducial markers are affixed to the top and side surfaces of each housing. Using these fiducial markers, the system achieves robust visual tracking, even under moderate occlusion or variable lighting conditions.

To ensure stable and repeatable placement of optical components, each unit is supported by a custom-designed base optimized for tabletop experimental environments. The bases are fabricated using fused deposition modeling (FDM) 3D printing with polylactic acid (PLA) filament. To prevent sliding and enhance frictional stability, each base is equipped with a rubberized bottom layer. Additionally, multiple neodymium magnets are embedded within the lower section of the base. The combined effect of the rubber and magnets significantly increases the frictional force between the base and the optical table, preventing unwanted sliding, tipping, and rotation under typical laboratory vibrations or minor external disturbances (e.g., those caused by the insertion of the fine-alignment tool).

### G. Robotic pick-and-place operations

The robotic arm executes pick-and-place operations by integrating global and local visual feedback with precise end-effector control. For each task, the system is first provided with the unique identifier corresponding to the desired optical component. The global stereo vision system, composed of two overhead 4K cameras, detects the ArUco markers affixed to the component’s casing and computes its  $(x, y)$  position and orientation relative to the optical table.

Following coarse localization, the robotic arm approaches the component using a pre-defined trajectory optimized to minimize collision risks. During the final approach phase, a sec-

ondary camera mounted on the robot’s end-effector provides high-resolution, close-range visual feedback. This enables fine alignment of the gripper with the standardized indentation designed into each casing, ensuring a secure and precise engagement during pickup.

Upon successful acquisition, the robotic system can perform a variety of manipulation tasks. These include translational movements along prescribed paths, such as following a laser beam propagation line, or rotational adjustments along the polar and azimuthal angles for component alignment. For placement operations, the system receives target  $(x, y)$  coordinates and orientation data. The robot translates the component to the desired location and gently deposits it onto the optical table.

Before finalizing placement, the end-effector camera performs a local verification and correction routine. Minor translational or rotational deviations are adjusted in situ to ensure alignment within the specified tolerance bounds. This dual-stage visual feedback—combining global position estimation with local fine correction—enables highly accurate, repeatable pick-and-place performance, which is critical for the assembly and realignment of complex optical experimental setups.

#### H. Correction of positional errors

Despite the high accuracy of the robotic placement system, occasional positional errors are observed. These inaccuracies arise from two primary sources: variable magnetic attraction between component bases and the optical table, and mechanical slippage at the gripper interface due to wear of the rubber contact pads.

To mitigate these errors and ensure reliable and robust assembly of setups, we implement an automated correction protocol based on post-placement verification. After each placement, the computer vision system re-evaluates the actual position of the optical element and compares it against the target coordinates. If the distance between the detected and intended positions exceeds a predefined tolerance threshold, the robot initiates a re-placement procedure. For all experiments reported in this work, we set this tolerance threshold to 0.5 mm.

This feedback-correction loop ensures that components are repositioned until they fall within the acceptable positional tolerance threshold. Empirically, most components require only a single placement attempt to meet this threshold. While this process may appear inefficient, the average placement time remains significantly lower than that of a human operator. Even with occasional multiple attempts, the robotic system maintains a net speed advantage, as human placement times typically exceed 20 seconds per component.

#### I. Fine alignment tool

The fine alignment tool is a compact, robot-deployable device designed to perform precision micro-adjustments on stan-

dard optical mounts (Figure 3b, Supplementary Video 9). The tool integrates an Arduino Nano microcontroller, a custom-designed printed circuit board (PCB) incorporating dual motor controllers, a camera module, and a dedicated illumination system. All components are enclosed in a 3D printed low-profile housing.

The embedded camera is centrally mounted within the housing of the tool and aligned coaxially with the tool’s mechanical axis. A ring of surface-mounted LEDs is positioned directly above the camera, providing uniform illumination and mitigating shadows from external light sources.

The core actuation mechanism consists of two custom-fabricated Allen keys that serve as precision interface tools for engaging standard optical component knobs. These Allen keys are machined from solid stock with a seamless transition between the shaft and tool head, forming a single integrated axle. The design was iteratively refined through multiple fabrication cycles, achieving sub-100  $\mu\text{m}$  tolerances. To minimize mechanical resistance and reduce power draw, the rotational axes are supported by high-performance bearings and shaft collars, ensuring stable alignment and preventing stalling during actuation.

The tool’s software stack utilizes asynchronous multi-threaded control, allowing the Arduino to operate independently of the primary robotic control system. This autonomy enables simultaneous translational and rotational movement, facilitating robust Allen key insertion even in cases of slight misalignment. The insertion routine leverages a helical approach, wherein the tool moves forward while rotating, effectively locating the socket with minimal mechanical stress.

To ensure secure disengagement, the system includes a micro-backdriving feature: upon completing an adjustment, the motors are rotated slightly in the reverse direction of the most recent turn. This subtle motion prevents mechanical binding and ensures smooth retraction of the Allen keys. The combination of precise motor control, low-friction mechanical design, and robust software architecture allows for reliable, repeatable fine adjustments across a variety of optical mounts and experimental configurations.

#### J. Optical measurements

For the fabrication of the multilayer photonic crystals (measured in Figure 4d), we employ plasma-enhanced chemical vapor deposition (PECVD) using the SAMCO PD-220 system to deposit a stack of silicon (Si) and silica ( $\text{SiO}_2$ ) layers onto a fused silica substrate (microscope coverslips of thickness 180 microns) with a deposition rate of approximately 55 nm/min for both materials. The deposition time is used to control the thicknesses of the individual layers. The photonic crystal consists of eight total layers, alternating between Si and  $\text{SiO}_2$ , each with a thickness of 40 nm except the fifth (Si) layer of thickness 110 nm which serves as a defect layer, creating a cavity. The simulated angle- and wavelength-resolved transmission spectrum is

calculated using the Rigorous Coupled Wave Analysis (RCWA) method, as implemented in Stanford Stratified Structure Solver ( $S^4$ ) [19]. In the simulations, the material model ( $n$ ,  $k$ ) for Si is

taken from Ref.[20] and fit to a fourth order polynomial in the wavelength range of 400-700 nm, while the index of  $\text{SiO}_2$  is assumed to be 1.45.

- 
- [1] H. Wang, T. Fu, Y. Du, W. Gao, K. Huang, Z. Liu, P. Chandak, S. Liu, P. Van Katwyk, A. Deac, *et al.*, Scientific discovery in the age of artificial intelligence, *Nature* **620**, 47 (2023).
- [2] C. Lu, C. Lu, R. T. Lange, J. Foerster, J. Clune, and D. Ha, The ai scientist: Towards fully automated open-ended scientific discovery, arXiv preprint arXiv:2408.06292 (2024).
- [3] M. Krenn, R. Pollice, S. Y. Guo, M. Aldeghi, A. Cervera-Lierta, P. Friederich, G. dos Passos Gomes, F. Häse, A. Jinich, A. Nigam, *et al.*, On scientific understanding with artificial intelligence, *Nature Reviews Physics* **4**, 761 (2022).
- [4] B. Burger, P. M. Maffettone, V. V. Gusev, C. M. Aitchison, Y. Bai, X. Wang, X. Li, B. M. Alston, B. Li, R. Clowes, *et al.*, A mobile robotic chemist, *Nature* **583**, 237 (2020).
- [5] T. Dai, S. Vijayakrishnan, F. T. Szczypiński, J.-F. Ayme, E. Simaei, T. Fellowes, R. Clowes, L. Kotopanov, C. E. Shields, Z. Zhou, *et al.*, Autonomous mobile robots for exploratory synthetic chemistry, *Nature* , 1 (2024).
- [6] K. Darvish, M. Skreta, Y. Zhao, N. Yoshikawa, S. Som, M. Bogdanovic, Y. Cao, H. Hao, H. Xu, A. Aspuru-Guzik, *et al.*, Organa: a robotic assistant for automated chemistry experimentation and characterization, *Matter* **8** (2025).
- [7] G. Tom, S. P. Schmid, S. G. Baird, Y. Cao, K. Darvish, H. Hao, S. Lo, S. Pablo-García, E. M. Rajaonson, M. Skreta, *et al.*, Self-driving laboratories for chemistry and materials science, *Chemical Reviews* **124**, 9633 (2024).
- [8] K. McCullough, T. Williams, K. Mingle, P. Jamshidi, and J. Lauterbach, High-throughput experimentation meets artificial intelligence: a new pathway to catalyst discovery, *Physical Chemistry Chemical Physics* **22**, 11174 (2020).
- [9] B. P. MacLeod, F. G. Parlane, T. D. Morrissey, F. Häse, L. M. Roch, K. E. Dettelbach, R. Moreira, L. P. Yunker, M. B. Rooney, J. R. Deeth, *et al.*, Self-driving laboratory for accelerated discovery of thin-film materials, *Science Advances* **6**, eaaz8867 (2020).
- [10] A. J. Mannix, A. Ye, S. H. Sung, A. Ray, F. Mujid, C. Park, M. Lee, J.-H. Kang, R. Shreiner, A. A. High, *et al.*, Robotic four-dimensional pixel assembly of van der waals solids, *Nature nanotechnology* **17**, 361 (2022).
- [11] I. Mandal, J. Soni, M. Zaki, M. M. Smedskjaer, K. Wondraczek, L. Wondraczek, N. N. Gosvami, and N. Krishnan, Autonomous microscopy experiments through large language model agents, arXiv preprint arXiv:2501.10385 (2024).
- [12] B. P. MacLeod, F. G. Parlane, C. C. Rupnow, K. E. Dettelbach, M. S. Elliott, T. D. Morrissey, T. H. Haley, O. Proskurin, M. B. Rooney, N. Taherimakhsoosi, *et al.*, A self-driving laboratory advances the pareto front for material properties, *Nature communications* **13**, 995 (2022).
- [13] C. Arnold, Cloud labs: where robots do the research, *Nature* **606**, 612 (2022).
- [14] M. Krenn, J. S. Kottmann, N. Tischler, and A. Aspuru-Guzik, Conceptual understanding through efficient automated design of quantum optical experiments, *Physical Review X* **11**, 031044 (2021).
- [15] M. Krenn, Y. Drori, and R. X. Adhikari, Digital discovery of interferometric gravitational wave detectors, *Physical Review X* **15**, 021012 (2025).
- [16] S. Arlt, H. Duan, F. Li, S. M. Xie, Y. Wu, and M. Krenn, Meta-designing quantum experiments with language models, arXiv preprint arXiv:2406.02470 (2024).
- [17] J. Landgraf, V. Peano, and F. Marquardt, Automated discovery of coupled-mode setups, *Physical Review X* **15**, 021038 (2025).
- [18] Z. Chen, R. Dangovski, C. Loh, O. Dugan, D. Luo, and M. Soljacic, Quanta: Efficient high-rank fine-tuning of llms with quantum-informed tensor adaptation, *Advances in Neural Information Processing Systems* **37**, 92210 (2024).
- [19] V. Liu and S. Fan,  $S^4$ : A free electromagnetic solver for layered periodic structures, *Comput. Phys. Commun.* **183**, 2233 (2012).
- [20] D. Franta, D. Nečas, L. Zajíčková, I. Ohlídal, J. Stuchlík, and D. Chvostová, Application of sum rule to the dispersion model of hydrogenated amorphous silicon, *Thin Solid Films* **539**, 233 (2013).